Catalysis Science & Technology

Accepted Manuscript

This article can be cited before page numbers have been issued, to do this please use: M. Potter, L. M. Armstrong and R. Raja, *Catal. Sci. Technol.*, 2018, DOI: 10.1039/C8CY01564C.

ROYAL SOCIETY OF CHEMISTRY

rsc.li/catalysis

View Article Online
DOI: 10.1039/C8CY01564C

Journal Name

ARTICLE

Combining catalysis and computational fluid dynamics towards improved process design for ethanol dehydration

Matthew E. Potter,*[a] Lindsay-Marie Armstrong*[a] and Robert Raja[a]

Received 00th January 20xx,
Accepted 00th January 20xx

DOI: 10.1039/x0xx00000x

www.rsc.org/

Through a combined computational fluid dynamics, characterization and catalysis study we have developed, for the first time, a working model of the ethanol dehydration process within a catalytic pelletized fixed bed reactor. The model, constructed from experimental kinetic data on the dehydration of ethanol to ethylene, with the industrial MTO catalyst SAPO-34, provides unique insights on reaction rate, product selectivity and local temperature fluctuations that are pivotal to reactor design towards optimized catalytic processes, and highly relevant for the optimization of industrial chemical processes.

Introduction

Mathematical modelling supports the understanding of various dynamic processes across multiple industrial sectors.[1] The multi-scale challenges surrounding porous catalytic environments includes capturing pore-scale flow and chemical phenomena, whilst simultaneously understanding the impact of meso-scale reactor design on mass and heat transfer through packed bed reactors. Upscaling for industrial-scale applications requires predicted models of the lower-scale dynamics since simultaneous resolution of all scales is far too computationally exhaustive, despite our advancing computational capabilities.

Quantum chemical approaches (such as Density Functional Theory; DFT),[2-4] and molecular dynamics,[5-7] are commonly used to investigate intrinsic catalytic properties, such as catalytic activity, selectivity and stability. This includes the adsorption and reaction mechanisms for ethanol dehydration and etherification on γ-Al_2O_3(100) and γ-Al_2O_3(111).[8,9] DFT studies have also explored the dehydration of ethanol on various surfaces such as α-Fe_2O_3[10] and HZSM-5.[11] As micro-scale approaches progress further to establish and understand the chemical interaction at the electronic and molecular scale, significant efforts are required to understand the meso- and macro-scale functionality of the catalysts in their operating environments.

Computational fluid dynamics (CFD) supports the prediction of complex flows using the mass, momentum and energy transport equations. It provides valuable insight into local dynamic properties such as pressures, temperatures and species compositions, which are crucial to catalytic performance. The modelling of flows through packed fixed bed reactors typically comes in two forms. The *discrete particle approach* resolves the conservation equations over a refined mesh, surrounding complex particle arrangements, to ascertain detailed flow and reaction dynamics in the near particles regions.[12] Whereas the *porous modelling approach* introduces volume fractions and effective source and sink terms to the conservation momentum equations to account for the influence of the porous medium in the flow, however this is at the cost of detailed micro-scale dynamics.[13]

Applications of CFD to catalytic processes is an evolving field of research where the multiscale approaches, capable of capturing the multiscale interchange, continues to expand. Extensive investigations have been made into understanding the flow and reaction dynamics within catalytic fixed bed reactors, typically using the discrete modelling approach.[14-16] The integration of microkinetic models into CFD for heterogeneous catalysts through the application of the operator-splitting-technique, using catalytic FOAM on the open-source OpenFOAM CFD code, has been applied to surfaces, such as solid reactor walls and interfaces between pellets and the surrounding environment.[14]

This method provides a fundamental multiscale approach of catalytic processes including transport through the surface boundary layer; diffusion through the porous structures; active site adsorption; chemical reaction; active site desorption; exiting pore diffusion; and finally exiting diffusion through the surface boundary layer into the bulk. Unfortunately capturing this degree of detail limits its applications to reactors with to low tube-to-particle diameter ratios as it requires significant refinement of the reactive wall regions or interface between a solid particle and the surrounding void.

CFD investigations also support the impact of varying reactor configuration, e.g., microchannel sizes within a square channelled microreactor, on the ethanol steam reformation over a Co_3O_4–ZnO catalyst;[17] and steam methane reformation

[a] University of Southampton, University Road, Highfield, Southampton, SO17 1BJ.
[b] Electronic Supplementary Information (ESI) available including experimental details, textural characterization of the acid catalyst, spectra from MAS NMR, CO probed FTIR and NH_3-TPD. Further catalytic data is also included along with computational details and parameters with numerical computational solutions. See DOI: 10.1039/x0xx00000x

within microreactors with varying geometric designs, namely microchannel and microslits.[18] These findings demonstrated that not only did the different surface-to-volume ratios impact the reactant conversion, but also that reactor design impacted the heat and mass transfer of reactants, and thus the overall catalytic performance. However, these were also based on reactive catalytic walls, rather than within packed bed reactors. For upscaling to large scale demonstrators and subsequently industrials applications such detailed microkinetic models are not feasible. Dixon[15] performed 3D CFD-based particle-resolved (PR) simulations of a randomly packed bed (0.68m length x 0.15m diameter) of 807 spherical catalyst particles with a tube-to-particle diameter ratio of 5.96. The method included fully coupled fluid flow to the transport and reaction within the catalyst particles, which required 51.9 million cells. This provided validation of the local transport parameters so they could explore scaling up the reactor design using 1D and 2D effective medium models of the steam methane reforming (SMR) process.

The computational element of this work will expand of these studies by developing an effective porous media model that considers catalytic flow through a reactor at the larger scale consisting of a higher tube-to-particle ratio that is directly validated with experimental data. This will promote the development of catalytic models for application at large scales which can subsequently support research into reactor design and optimisation.

A multi-scale, dynamic, two-dimensional, heterogeneous model for catalytic steam methane reforming (SMR) is developed by Ghouse and Adams.[19] This incorporated a diffusion-limited model that was not based on the use of an effectiveness factor. Petera *et al.*[20] proposed a universal coupling of macro- and micro-geometries represented by two finite element meshes system. A macro-scale mesh was associated with the reactor as a porous bed and a microscale mesh for a representative collection of catalyst pellets located at the nodal points of the macro-mesh. The method was applied to methanol synthesis in an industrial fixed bed reactor, however, the concentrations were not validated against experimental data for that scale reactor. They did however show some verification against the lab-scale work of Vanden Busche and Froment,[21] since their kinetic model was used in the multi-mesh approach.

In our previous experimental work we described our targeted approach to designing a solid-acid heterogeneous catalyst for this process. By isomorphous incorporation of small quantities of dopant species within a microporous aluminophosphate framework, highly active and selective Brønsted acid sites were generated, affording near-quantitative yields of ethylene at temperatures as low as 300 ^{o}C.[22,23] We found that the industrially deployed Methanol To Olefins (MTO) catalyst, silicon substituted aluminophosphate, SAPO-34, was particularly effective. This was attributed to a combination of isolated strong Brønsted acid sites, favoring the selective formation of ethylene, within a chabazite (CHA) framework (possessing a pore diameter of just 3.8 Å) that bestows *product selectivity* on the reaction.[23] A large body of work has been dedicated to understanding the mechanism for this reaction, using a range of solid acid catalysts.[24-28] The precise mechanism is still under debate, particularly on the role of diethyl ether ($C_4H_{10}O$). Typically, targeted improvements have been made to the active site, or framework of the solid-acid catalyst to optimize ethylene (C_2H_4) yield.

Whilst computational porous models have been applied to catalytic processes previously for the conversion of carbon monoxide to diethyl oxalate,[29] and for the dehydrogenation of syngas in a fixed bed reactor which compared reasonably with experimental data;[30] to the best of our knowledge, such approach has not been taken to investigation the dehydration of ethanol for the production of ethylene. However, scarce few examples exist where the fluid dynamics of such a process has been investigated in combination with the catalysis to build a model for optimizing reactor design at the larger scale.

In this work we present a combined CFD-catalysis porous media model aimed at fully understanding the catalytic process of the dehydration of ethanol into ethylene, using a fixed-bed reactor. This study is aimed at extending our understanding beyond simple reaction kinetics, with a view to expanding our knowledge on molecular interactions at the mesoscale, for the process as a whole. In doing so, we highlight how CFD can guide experimental optimization of catalytic processes. In order to construct the CFD model we first derive quantifiable parameters such as reaction rate, activation energy and product distribution. This is achieved through a kinetic study of the catalytic dehydration of ethanol, with our SAPO-34 catalyst. Once determined, these findings serve as inputs for the CFD model, and help validate the accuracy of our model. The CFD model that we have devised then allows us to explore, in greater detail, localized variations in the catalyst bed, such as differences in concentration and temperature changes as the reaction progresses. The scope for extending similar validated models will be beneficial to the catalytic community for optimizing a range of industrial processes.

Experimental Results

Catalyst Integrity

SAPO-34 was synthesized according to previous literature procedures for the use in ethanol dehydration.[22,23] Powder X-ray diffraction (XRD, Figure S1) confirmed that the sample was highly crystalline and that CHA (Chabazite) was the only crystalline phase observed, with unit cell parameters (Table S1) of a and b falling in the range of 13.7 – 13.8 Å, with c = 15.0 Å ($\alpha = \beta = 90^{o}$ and $\gamma = 120^{o}$).[22,23,31,32] Similarly the surface area and pore volume were in good agreement with previous literature at 580 $m^2\ g^{-1}$, with micropore volume of 0.27 $cm^3\ g^{-1}$, and total pore volume of 0.33 $cm^3\ g^{-1}$.[31,32] ICP analysis of the sample showed a silicon loading of 3.4 wt% (Table S1), corresponding to a maximum possible acidity of 1.2 mmol/g. Scanning electron microscopy (Figure S2) confirmed the majority of the particles were cubic of 1 μm in size. While smaller particles (0.1 – 0.2 μm) can be seen, these constitute a small minority.[22]

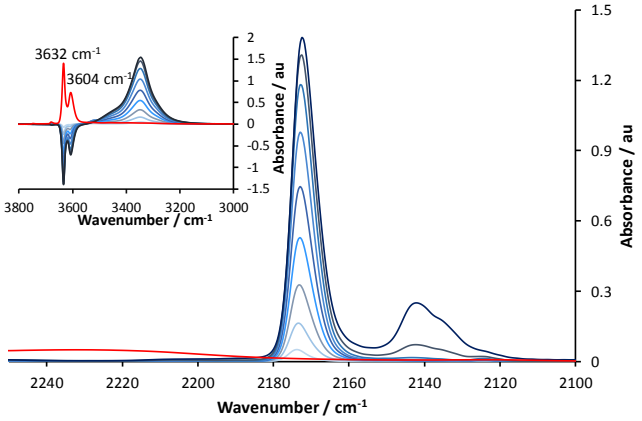

Figure 1. FT-IR spectra of the CO region of undoped, bare SAPO-34 framework (red) and the difference spectra on sequentially adding 0.2 cm^3 of CO in 0.02 cm^3 increments (from light to dark blue). Inset: FT-IR spectra of the hydroxyl region under identical conditions.

Solid state NMR experiments confirmed the AlPO structure, as ^{31}P MAS NMR (Figure S3) showed a single peak at -26 ppm, attributed to $P(OAl)_4$.[22,33] ^{27}Al spectra (Figure S4) showed a primary peak at 33 ppm, attributed to $Al(OP)_4$, with a further peak at 8 ppm, previously assigned to hydrated SAPO-34, as $Al(OP)_4(H_2O)$.[22,33] ^{29}Si NMR (Figure S5) probed the isomorphous substitution of silicon into the framework, with a primary peak at -95 ppm, attributed to $Si(OAl)_4$, indicative of type II substitution of silicon into the framework.[22,33] Shoulder peaks were also seen at -115 and -100 ppm, attributed to $Si(OSi)_4$ and $Si(OSi)_2(OAl)_2$, which occur due to the formation of silicon islands (non-isolated sites).[22,33]

The acidity of the system was found to be in good agreement with previously published literature. NH_3-TPD (Figure S6, Table S2) showed a prominent feature with a maxima at 447 °C, with a total acidity of 0.82 mmol g^{-1}.[34] This is lower than the theoretical maximum (1.2 mmol g^{-1}), due to the silicon islanding observed in the ^{29}Si NMR. The acidity of SAPO-34 was investigated through the use of CO-probed FT-IR (Figure 1). The pre-treated bare SAPO-34 showed the characteristic two hydroxyl species (3632 and 3604 cm^{-1}). These correspond to two different OH positions, representing protons attached to the O4 oxygen, residing in the 6 rings (3632 cm^{-1}) and protons attached to the O2 oxygens residing in the 6-6 rings (3604 cm^{-1}).[35-37] Also a hydroxyl band is present at 3678 cm^{-1} and can be attributed to ubiquitous P-OH surface defects. On adsorbing CO onto the sample, both hydroxyl groups are completely removed, showing that all the OH species are accessible to CO.[35-37] The 3632 and 3604 cm^{-1} peaks shifted by a value of 286 and 329 cm^{-1} respectively, showing the different signals have diverse acidity, with the 3604 cm^{-1} peak being slightly more acidic.[35-37] The depletion of the hydroxyl bands was also seen by the appearance of a peak at 2172 cm^{-1}, attributed to hydrogen bonded CO. A second band was seen at 2141 cm^{-1}, attributed to physisorbed CO on the surface of the SAPO-34.[35-37]

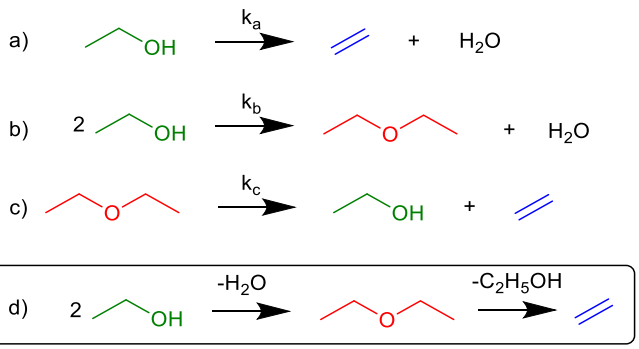

Scheme 1. Suggested reaction pathways for the dehydration of ethanol to ethylene.

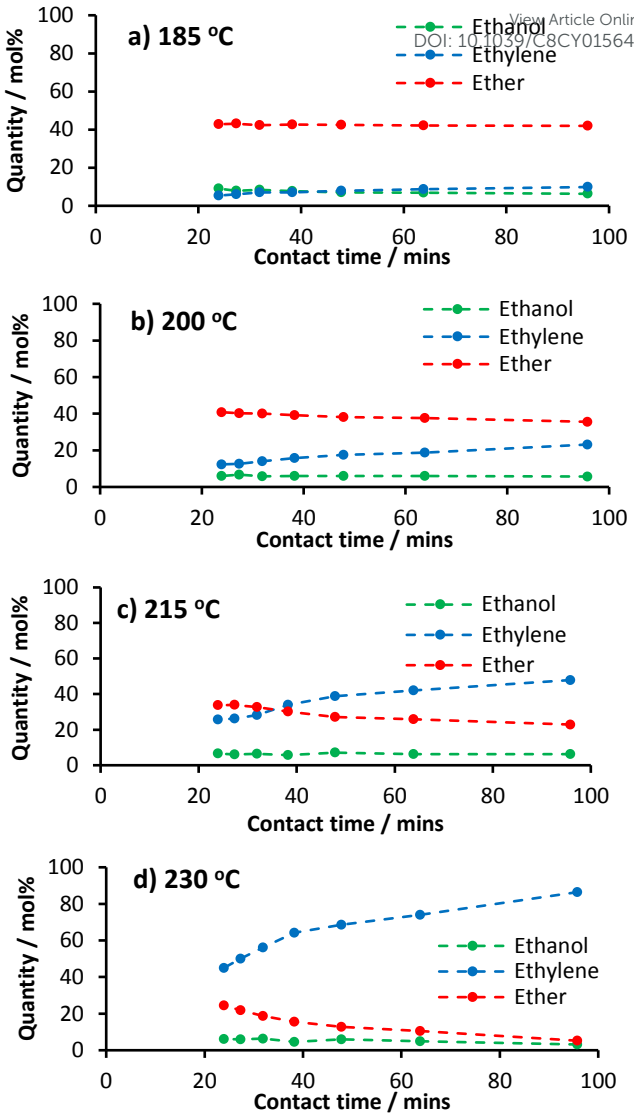

Figure 2. The influence of contact time on product distribution for ethanol dehydration with SAPO-34, 25 ml/min of Helium carrier gas, with a liquid feed of 10% heptane (standard) in ethanol at a) 185 °C, b) 200 °C, c) 215 °C and d) 230 °C.

Acid Catalysed dehydration of ethanol

SAPO-34 has previously been shown to be a stable, (Figure S7) active catalyst for the acid-catalyzed dehydration of ethanol

(C_2H_5OH) to ethylene (C_2H_4) at low (< 250 °C) temperatures; it is therefore is an ideal candidate for use as our model catalyst. In our previous work,[22,23] and in the wider literature,[24-28,38-40] the dehydration of C_2H_5OH to C_2H_4 proceeds through three main reaction pathways (scheme 1); a – direct formation of C_2H_4 from C_2H_5OH, b – dehydration of C_2H_5OH to form $C_4H_{10}O$ and c – degradation of $C_4H_{10}O$ to give C_2H_4 and C_2H_5OH. Our preliminary studies have suggested that $C_4H_{10}O$ is not a competing by-product, rather an intermediate for the formation of C_2H_4 (following reaction b then reaction c). Previous work on γ-Al_2O_3 suggests a fourth pathway is possible where $C_4H_{10}O$ is cleaved to give two moles of C_2H_4 and one mole of H_2O, however this was found to have little influence on the kinetics of the reaction below 250 °C,[24-28] and was considered for this work, but did not show any significant differences in the computed reaction profile.

To investigate the reaction kinetics the substrate (C_2H_5OH) flow rate was varied to generate a kinetic plot at four different temperatures (185, 200, 215 and 230 °C), over a range of WHSV's from 0.5 to 2.0 hr^{-1} (Figure 2), corresponding to contact times between 100 and 20 minutes (respectively, owing to the inverse correlation between WHSV and contact time). The quantity of C_2H_5OH was found to be less than 5 mol% in almost all cases, showing that it is rapidly consumed in the reaction. The main variant within this data set is the change in product distribution between $C_4H_{10}O$ and C_2H_4. At lower temperatures and fast contact time (higher WHSV) $C_4H_{10}O$ is the favored product, with the fraction of C_2H_4 increasing with higher temperatures and lower contact times. If the proposed mechanism is correct (scheme 1), the variation in product distribution suggests that the latter reaction (scheme 1, reaction c) occurs at a slower rate than the formation of $C_4H_{10}O$ from C_2H_5OH, as shown by the high yields of $C_4H_{10}O$ at low temperatures and high contact times. It is noted that no other products were observed, which we attribute to the uniformity of acid sites in the catalyst, and the constricting pore size enforcing product selectivity, limiting oligomerization.[22,23]

The product distributions, varying as a function of contact time, were used as inputs to calculate the rate constants of the three reactions, at the different temperatures and flow rates. As highlighted previously, there is a plethora of investigations into the mechanisms and pathways involved with these reactions. Zhang and Yu[24] suggested that reaction b (a bimolecular nucleophilic substitution reaction), was a second-order reaction. This was also supported by Bokade and Yadav[41] who concluded the dehydration of both ethanol (reaction b) and cracking of diethyl ether (reaction c) were second-order reactions using a heteropolyacid. We considered these reaction orders in our model for establishing the rate constants which were predicted using the open-source software Copasi[42].

The software takes the concentrations of the chemical species as a function of time, and the expected chemical equations, as an input. The rate of each reaction was given by a kinetic rate law (of order 1, 2 and 2 for reactions a, b and c, respectively, as discussed above) and the kinetic rate constants were established using a parameter estimation which models the three different proposed reactions simultaneously, with inputs from all data sets from the different operating temperatures and flow rates, and minimizes the value distances between the model and experimental data. We initially applied a genetic algorithm[43] before performing the local optimisation by Levenberg-Marquardt, which is a least-squares approach to solving non-linear problems.[44,45]

Table 1. Calculated activation energies and pre-exponential factors for the reactions.

Rate constant	E_a/(kJ mol^{-1})	ln(A*)
k_a	65.58	8.12
k_b	70.73	24.77
k_c	142.70	39.96

*A varies in units due to the difference in reaction order of the reactions, for k_a (first order) A has units sec^{-1}, for k_b and k_c (both second order) A has units of ml mol^{-1} sec^{-1}.

We present the individual rate constants established using the multi-set data for the different experimental cases in Table S3. We consider the individual cases to ascertain whether any reactions are kinetically limited (constant with varying WHSV) or diffusion limited (varying with WHSV). As shown in Figure S8 the rate constants from reaction b (ether formation) were found to be constant with respect to flow rate, showing that the reaction is kinetically limited, and not diffusion limited. Therefore any thermodynamic data relating to reaction b will relate to the chemical transformation, and external diffusion can be excluded. In contrast the rate constants calculated for reaction c (ether dehydration), in Figure S9, decrease with increasing flow, before converging at higher WHSV (1.75 and 2.0 hr^{-1}). This suggests the reaction is diffusion limited at lower flow rates. The rate constants from reaction a (ethanol directly to ethylene, Figure S10) showed variation at higher temperatures, however despite this the contribution of this reaction was found to be negligible in the overall process when considering the reaction rates, thus any errors have limited influence on the overall kinetic model. The variation of k_c is in line with our previous observations that ether diffusion is limited in the pores of SAPO-34.[23] This is explained as the activation energy for diffusion is typically much lower (< 15 kJ/mol) than chemical activation energies, leading to the larger rate constants observed at low flow rates for reaction c. In contrast, the smaller ethanol molecule can diffuse more freely through the SAPO-34 pore networks, thus reaction b is not constrained by diffusion. The convergence of the rate constant at higher flows shows the reaction is becoming chemically limited, likely due to shorter contact time leading to the formation of fewer ethoxy intermediates.[23] Therefore we use only the kinetic rate constant values for the two WHSVs (1.75 and 2.0 hr^{-1}) to extract the activation energy and pre-exponential factors (Table 1) with an Arrhenius plot (Figure S11) for reaction c. As at this point it is assumed the reaction is no longer limited by external diffusion.

Computational investigation

Model development

Two-dimensional computational fluid dynamics (CFD) simulations were performed using a reactive porous media model in ANSYS Fluent 17.1.[46] Figure S12 provides the schematic for the experimental packed bed. The computational

domain focused solely on the catalytic zone based on the following assumptions:

1. The reactants are assumed to be pre-mixed, heated and entering as a steady flow through the inlet of the catalytic zone.
2. A single gaseous mixture could be simulated since the liquid solutions would have vaporized under those conditions, thus alleviating additional multi-phase complexities.
3. The catalytic region is the only reactive zone; hence the other regions would not directly impact the final compositions.

The cylindrical catalytic bed of the reactor (4 mm diameter and 5 mm height) was discretized into 40000 quadrilateral cells. A constant wall temperature was set of either 185, 200, 215 or 230 °C to align with the experimental conditions. The walls were defined as no-slip boundary conditions. The bed is initially assumed to have a uniform temperature and operating at atmospheric pressure to align with experimental operating conditions. The model accounts for temperature variation due to endo- and exothermic reactions. A mass flow inlet defined the mass flow rates of ethanol, heptane and helium for a range of WHSV from 0.5 to 2.0 hr^{-1}. The mass flow rates are presented in Table S4. The temperature of the gases entering the reactor was set to the corresponding temperature of the reactor bed, which was fixed for that case (either 185, 200, 215 or 230 °C). The outlet was defined as an outflow boundary conditions. The inlet and outlet boundaries were set to atmospheric pressure to align with the experimental set up.

The CFD reactive porous model is expanded using User-defined Functions (UDFs) to incorporate a range of a parameters that are either fundamental constants, or derived experimentally (Table S5) into the transport equations. The catalytic loading was calculated based on the SAPO-34 surface-to-volume ratio from the experiments, therefore accounting for the area a reaction can take place in, for each cell, by multiplying the volume of the discretized cell by this ratio. This value was calculated to be 1.76 x 10^9 m^{-1} (surface area 580 m^2 g^{-1}, total pore volume 0.33 cm^3 g^{-1}). The average pellet diameter (1 µm) was estimated from the SEM images, and a bed porosity of $\varepsilon = 0.4$ was used to account for a randomized distribution within the bed of roughly cubic shaped pellets.[47] A flow resistance was applied to the pelletized catalytic region which accounts for the viscous and inertial losses experienced within the packed pellet bed. These parameters were determined according to the semi-empirical Ergun equation for pressure drops within packed beds.[48] Table S5 provides the full simulation input parameters. The pressure and velocity were coupled by the SIMPLE algorithm.[49] Initially the impact of temperature on ethanol dehydration was investigated using a constant WHSV of 2.0 hr^{-1}. Similarly the influence of varying the WHSV was investigated at a fixed temperature of 200 °C. Table S6 defines the different computational investigations performed.

Effect of temperature variation

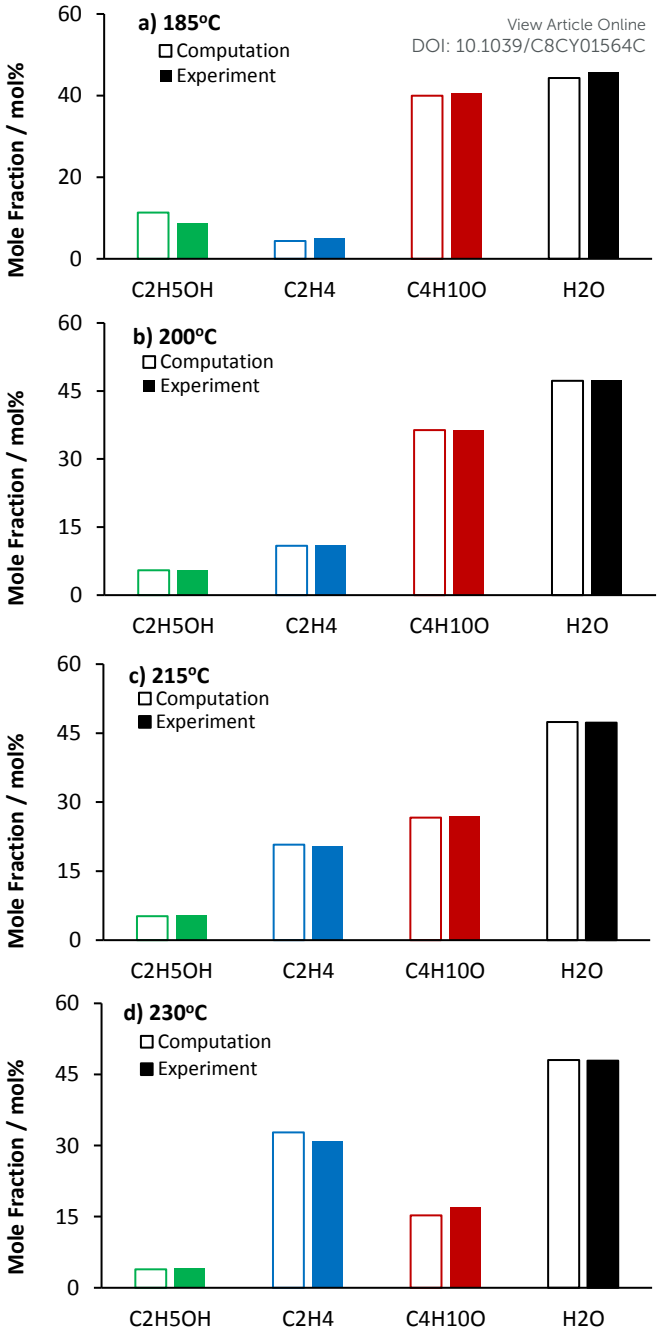

Figure 3. Comparison of computational and experimental exiting mole fractions for 2.0 hr^{-1} WHSV for increasing reactor temperature, a-d representing 185, 200, 215 and 230 °C, respectively.

Table S7 and Figure 3 provides the simulated exiting molar concentrations and mole fractions for $C_4H_{10}O$, C_2H_4, C_2H_5OH and H_2O alongside the corresponding experimental investigations for varying operating temperatures at 2.0 hr^{-1}. As shown there is excellent agreement between the computational mole fractions and the experimental data. The molar concentrations are slightly under predicted but within a similar magnitude to the experimental concentrations. Subtle variations between experimental and predicted results are likely due to the estimated parameters (ε, $1/\alpha$, C_2) which are difficult to accurately ascertain from the experiments, e.g., porosity distribution within the bed, etc.

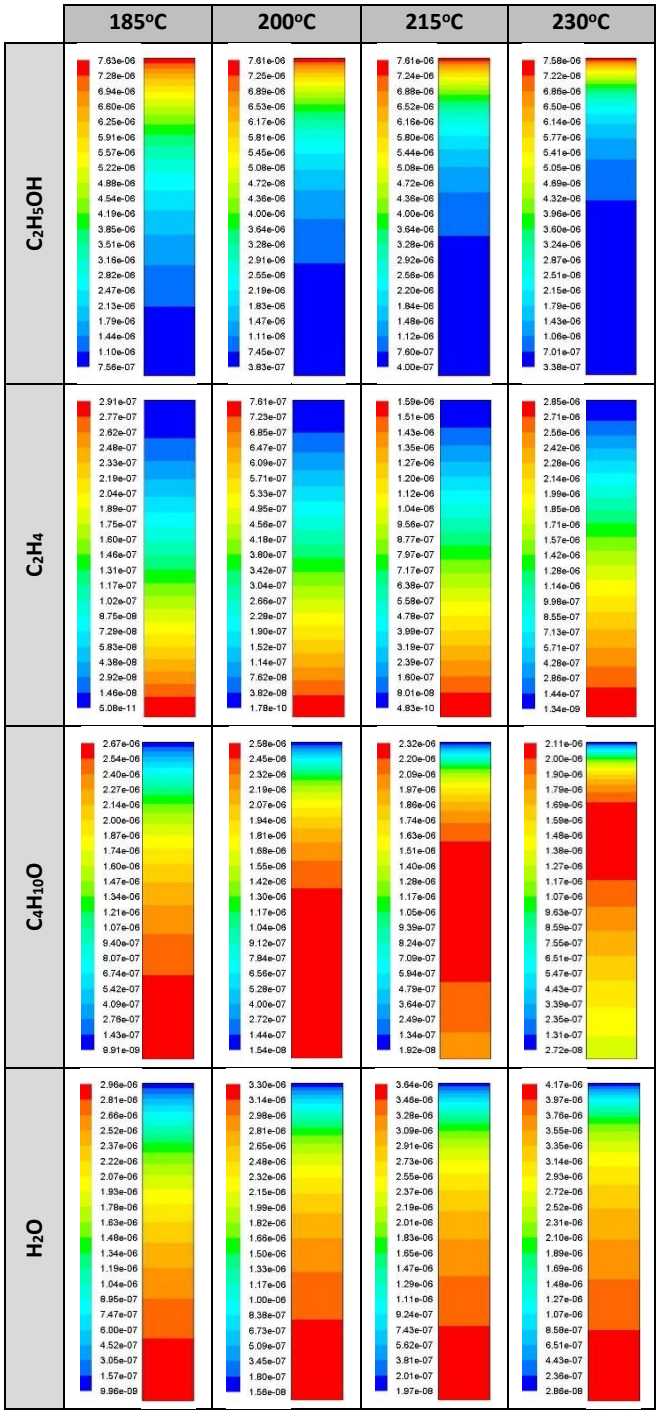

Figure 4. Molar concentration (mol cm^{-3}) distribution of species at varying temperatures for 2.0 WHSV (hr^{-1}) with varying reactor height (y-axis), as the chemicals are introduced at the top of the reactor and exit through the bottom.

Figure 4 shows contour plots of the molar concentrations of each species varying within the fixed bed system from the inlet (top) to the outlet (bottom) for the 2.0 hr^{-1} WHSV case. Initial observations show a progressive increase in concentration of H_2O and C_2H_4 down the bed, with virtually no C_2H_4 present at the top. Increased temperature further promotes the amount of both products. The contour plot for $C_4H_{10}O$ shows a different trend where the highest molar concentration of $C_4H_{10}O$ actually decreases with increasing temperature. Furthermore, the maximum concentrations are reached progressively higher up the bed for increasing temperatures before decreasing further down the bed at the higher temperatures. This further vindicates the mechanistic inference made in our previous studies,[22,23] thus confirming the formation of $C_4H_{10}O$ as a reaction intermediate.

Figure 5 shows a general downward trend of molar concentration for $C_4H_{10}O$ with increasing temperature whilst the product C_2H_4 increases steadily. This is expected given the influence of temperature on the Arrhenius reaction rates. The magnitude of the computational values compares well with the experimental data, although the molar concentrations are

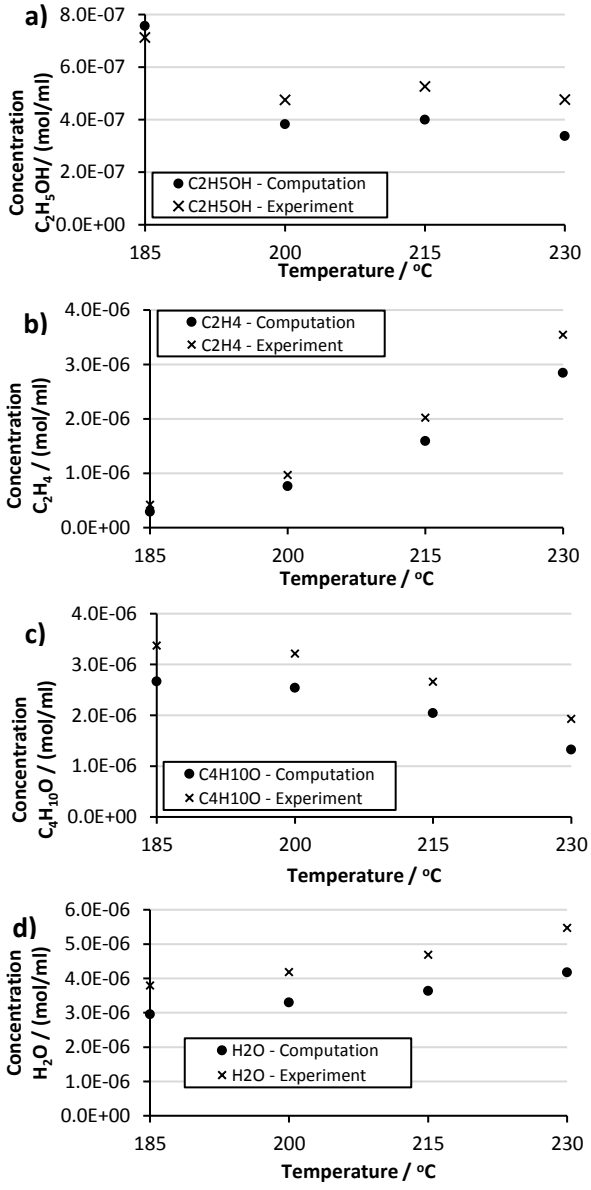

Figure 5. Comparison of computational and experimental exiting molar concentrations (mol/ml) for 2.0 hr^{-1} WHSV for increasing reactor temperature between 185, 200, 215 and 230 °C, for a) C_2H_5OH, b) C_2H_4, c) $C_4H_{10}O$ and d) H_2O.

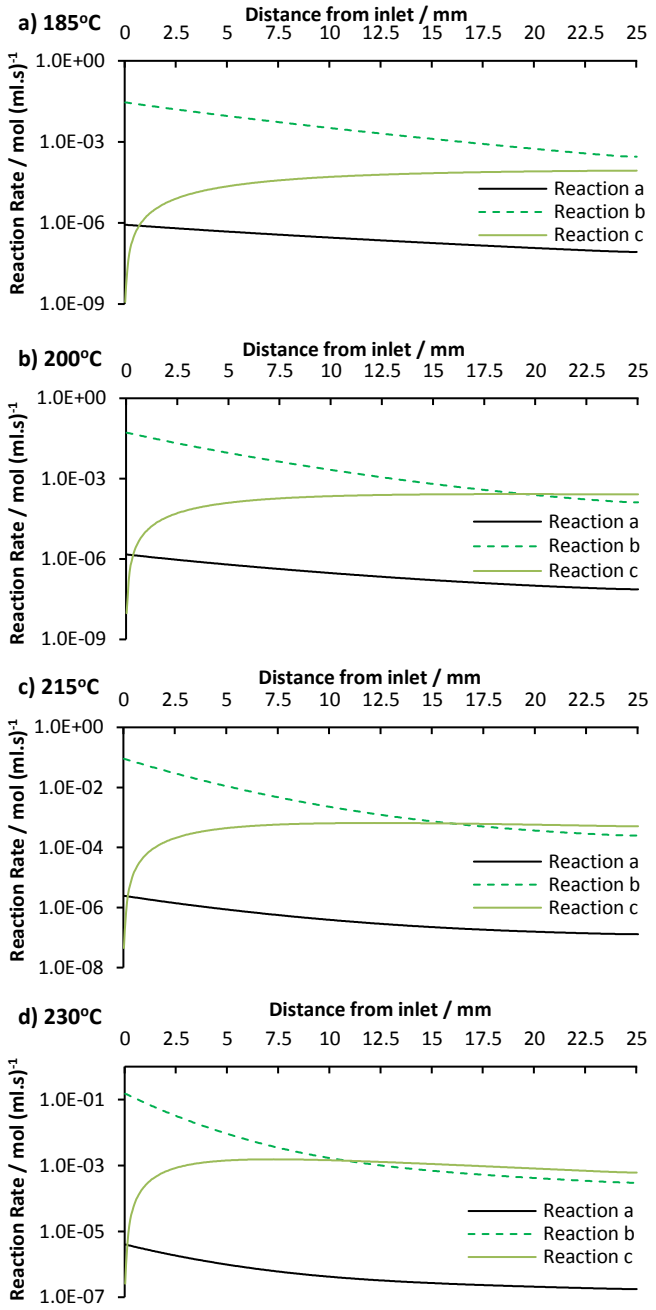

Figure 6. Reaction rates (mol (ml.s)$^{-1}$) for individual reactions over varying operating temperatures (°C) for the 2.0 hr^{-1} WHSV case.

slightly under predicted and slight deviations can be seen to increase with temperature. It is likely that the accelerated reaction rates at higher temperatures coupled with any numerical errors resulting from estimated parameters could influence the local heat and mass transfer. Thus reinforcing the need to pursue research into more detailed experimental analysis, and the subsequent impact of porosity and diffusion/inertial resistances.

A key transition point is observed both experimentally and computationally between the temperatures of 215 and 230 °C whereby the mole fractions and concentrations presented in Figure 3 and Table S7, respectively, starts to switch from $C_4H_{10}O$ to C_2H_4 as the predominant product after H_2O. It is this role of $C_4H_{10}O$ being a reaction intermediate that results in $C_4H_{10}O$ degradation taking place higher up the bed producing C_2H_5OH and C_2H_4 (scheme 1, reaction c). A more complex relationship can be observed, whereby it is possible for more ethanol to be produced than is being consumed. This is observed near the temperature range of this transition point, both experimentally and numerically, in Figure 5 where the molar concentration of C_2H_5OH increases slightly at 215 °C. This is due to the outlet being located immediately below the peak $C_4H_{10}O$ region where C_2H_5OH is still higher due to being a product of reaction c yet has not had sufficient time to degrade further via reaction b.

Figure 6 shows the reaction rates as a function of bed depth based on their local temperatures and reactant concentrations. Whilst the production of $C_4H_{10}O$ from reaction b (and direct C_2H_4 production from reaction a) consistently decreases down the bed, due to the continual conversion of C_2H_5OH; the concentration of $C_4H_{10}O$ increases down the bed, reaches a maxima in $C_4H_{10}O$ concentration before decreasing. With increasing temperatures the degradation of $C_4H_{10}O$ from reaction c exceeds the reaction rate of reaction b higher up the bed due to the higher concentrations of $C_4H_{10}O$. Reaction a seems to have a negligible influence, although it can be noted that at the lower temperatures it exceeds Reaction b at the top of the reactor where C_2H_5OH is more prevalent.

Further observation of the rate constants, k_b and k_c, over increasing temperatures (Figure S13) shows that although k_b dominates the two reactions, it is the increasing rate, k_c, that is crucial for the enhanced production of C_2H_4 and simultaneous degradation of $C_4H_{10}O$. As reaction c has both a high activation energy (142.70 kJ mol^{-1}) and high pre-exponential factor ($e^{39.96}$ s^{-1}), it is highly susceptible to changes in temperature, as seen in Figures S9 and S13, where the rate constant undergoes almost a 30 fold increase from 185 to 230 °C at WHSV 2.0 hr^{-1}.

CFD provides valuable insight of localized temperature within the catalyst bed, something that is difficult to ascertain experimentally. We observe subtle fluctuations in relative bed

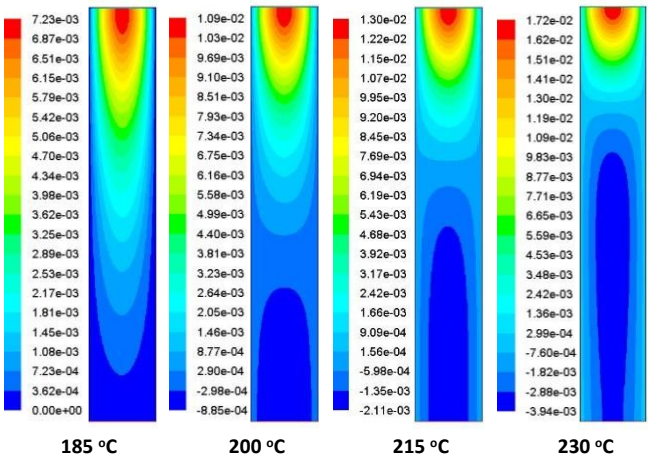

Figure 7. Relative temperature distributions (in °C) within the reactor for varying operating temperatures, at a WHSV of 2.0 hr^{-1}.

temperature ($T - T_{operating}$), i.e., positive values indicate an increase in temperature and vice versa (Figure 7), due to the modeling of the total energy which incorporates the enthalpy of the species (page S13, Eqn 12). For all four operating temperatures, the highest temperatures are observed near the inlet of the catalyst bed. This is primarily due to the exothermic formation of H_2O and $C_4H_{10}O$ from two moles of C_2H_5OH (scheme 1, reaction b), which happens rapidly in all cases at the top of the bed. This further justifies the rapid depletion of C_2H_5OH near inlet of the bed in figure 4 for all temperatures. In contrast the degradation of $C_4H_{10}O$ to C_2H_4 and C_2H_5OH (scheme1, reaction c) is an endothermic process, leading to negative local temperatures.

For all operating temperatures the lowest temperatures observed align with the location where $C_4H_{10}O$ reaches a maximum in figure 4. Thus further vindicating that the rate of the endothermic degradation of $C_4H_{10}O$ peaks in these regions, as suggested in figure 6. It should be noted that the local temperature variations within the catalyst bed (± 2 x 10^{-2} °C) are not sufficient to have any notable influence on the kinetics of the reaction, as the variations observed in this study are subtle. Insight of the temperature profiles from the CFD suggests that it is likely the competing endothermic and exothermic reactions are cancelling each other to maintain minimal overall temperature change; although it should also be noted that dilute quantities of C_2H_5OH being introduced would also lead to minimal temperature change. However this level of detail highlights the potential of a combined CFD catalysis approach for investigating detailed changes in both thermodynamics and reaction kinetics on a larger scale.

Effects of increased WHSV

Figure 8 and Table S8 shows the mole fractions and concentrations of the exiting species for varying WHSV at operating conditions of 200 °C and 230 °C. The porous model simulated the range of WHSVs using the kinetically limited rate constants. The CFD results (Figure 8) confirms the expected under prediction of the degradation of $C_4H_{10}O$ at the lower WHSV cases. This subsequently led to lower concentrations of C_2H_4 being produced. Increasing the flow rate to 1.75 hr^{-1} and 2.0 hr^{-1} led to very good agreement with the experimental results. This supports our assumption that reaction c is a diffusion-kinetic limited reaction, whereby a suitable model for the diffusion behavior needs to be incorporated to capture the transition across flow rates.

Given that reaction a is negligible, H_2O is predominantly being produced via reaction b. Since the H_2O values compare well across all flow rates this suggests that the kinetics rates for reaction b are well represented thus supporting the validation of the model for this reaction. The slight deviations in C_2H_5OH, particularly at the higher temperatures, are likely due to it being a product of reaction c which we showed as being generally underperforming. However, these are of similar magnitudes with the experimental data and with the low concentration of C_2H_5OH experimentally we recognized the potential deviations are likely. Increasing the temperature further promotes the

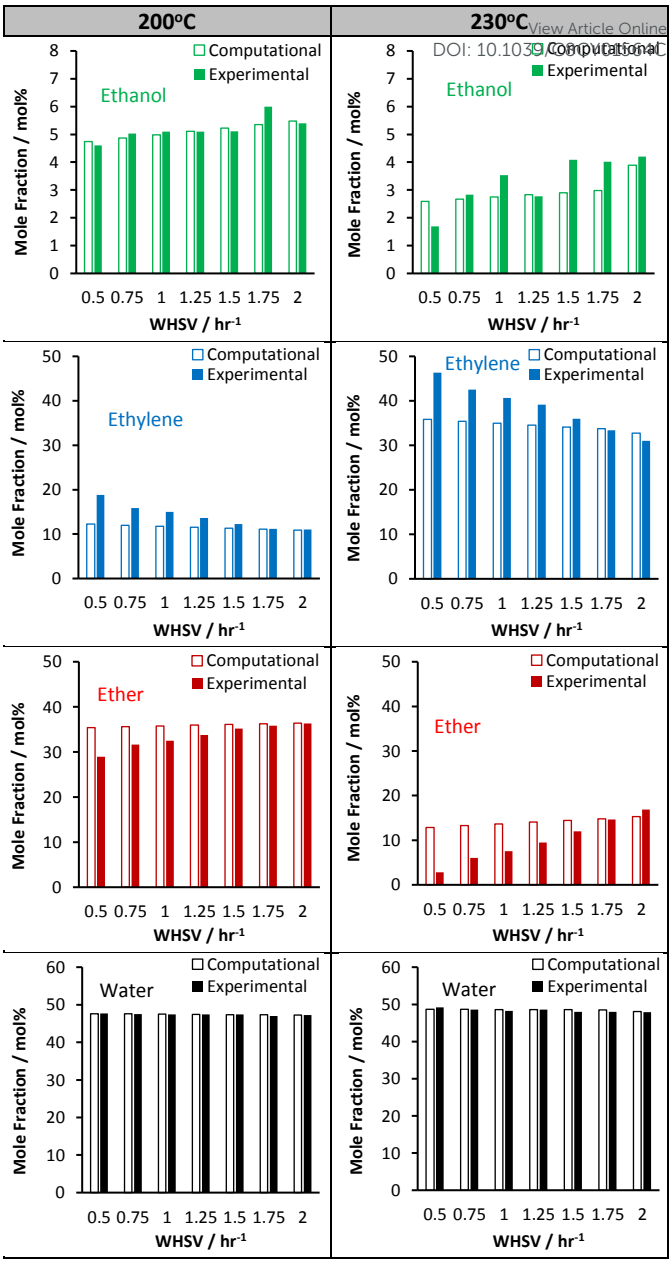

Figure 8. Comparison of computational and experimental exiting mole fractions for varying mass flow rates (WHSV), 0. 5 - 2.0 hr^{-1} at 200 °C and 230 °C for a) C_2H_5OH (green), b) C_2H_4 (blue), c) $C_4H_{10}O$ (red) and d) H_2O (black).

deviation between computational and experimental results. This is expected given the impact temperature play on the reaction kinetics.

Another factor for consideration is that various modelling assumptions may also have an impact. If the models are too simplified increased concentrations of the C_2H_5OH could propagate further into the catalyst bed thus delaying the subsequent $C_4H_{10}O$ (scheme 1, reaction c) and competing direct formation of C_2H_4 from C_2H_5OH (scheme 1, reaction a) leading to an over prediction of reactants and under predictions of the products at the outlet. Thus reinforcing the need to develop further models that are susceptible to the sensitive environment of catalytic processes. For example, incorporation

of realistic effects such as pore contamination at different temperatures for the meso-scale.

Having computational insight into the local flow and reaction dynamics within the catalyst bed supports the optimization of experimental set up and reactor design to maximize performance. Ongoing research to further enhance our understanding of the processes and maximize performance includes:

- *establish the kinetic-diffusion reaction kinetics for the dehydration of $C_4H_{10}O$ (scheme 1, reaction c):* This will allow models to incorporate the transition between diffusion-limited and chemical-limited conditions over a range of flow rates;
- *implementing more detailed porous-scale averaging models:* to incorporate additional physical processes which will potentially maximize exposure of reactants to catalytic sites;
- *exploring pellet properties and arrangements:* to understand the impact of flow propagation, localized temperatures and subsequent impact on species formation under different operating conditions;
- *CFD aided reactor design:* through the investigation of geometric parameters to ensure sufficient residence times to maximize C_2H_4; or to promote heat and mass transfer more effectively.

Obtaining a detailed understanding of these phenomena, which are otherwise not readily discernible and amenable using *operando* experimental techniques, augurs well for the scaling up of catalytic reactors in the future.

Conclusions

Through a combination of catalysis and computational fluid dynamics we have developed, and validated a functional CFD porous media model of the acid catalyzed dehydration of ethanol to ethylene, which can now guide improvements to our catalytic reactor towards improved yields of ethylene. By methodically varying the reaction parameters in our continuous catalytic fixed bed flow reactor we are able to calculate experimental parameters for the reaction kinetics to serve as inputs for our CFD model. From our findings we propose that the dehydration of $C_4H_{10}O$ is a kinetic-diffusion reaction, which offers significant potential to further research. Furthermore, vindicate the mechanistic inferences made in our previous studies,[22,23] that $C_4H_{10}O$ forms as a reaction intermediate. The model was validated against experimental data, and provided powerful insights on local concentrations and temperatures which could not otherwise be obtained. These insights are now able to steer reactor design, upscaling and adaption of similar models for processes. Whilst operando spectroscopy has played a significant role in the past decade for understanding molecular aspects relating to catalyst design and for establishing structure-property correlations, the prospects for using CFD to optimize reactor design based on mesoscale modelling of reaction intermediates, can pave the way for deploying existing industrial catalysts (such as the MTO catalysts in this case) for new applications (such as ethanol dehydration), by judicious manipulation and optimization of reactor engineering technology. We believe similar techniques and studies would be widely applicable and beneficial to a plethora of catalytic processes.

Conflicts of interest

There are no conflicts to declare.

Acknowledgements

This work was funded by the EPSRC under the grant: “Adventures in Energy”, EP/N013883/1; 2016-2018.

Notes and references

1 M. Griebel, S. Knapek and G. Zumbusch, Numerical simulation in molecular dynamics: numerics, algorithms, parallelization, applications, Springer, Heidelberg, 2009.
2 L. Gomez-Hortiguela, F. Cora’, C. R. A. Catlow, *ACS. Catal.*, 2011, **1**, 18.
3 S. Kuld, M. Thorhauge, H. Falsig, C.F. Elkjaer, S. Helveg, I. Chorkendorff and J. Sehested, *Science*, 2016, **352**, 969.
4 A. A. Latimer, A. R. Kulkarni, H. Aljama, J. H. Montoya, J. S. Yoo, C. Tsai, F. Abild-Pedersen, F. Studt and J. K. Norskov, *Nature Mater.*, 2017, **16**, 225.
5 K. C. Kim, E. G. Moschetta, C. W. Jones and S. S. Jang, *J. Am. Chem. Soc.*, 2016, **138**, 7664.
6 S. L. C. Moors, K. De Wispelaere, J. Van der Mynsbrugge, M. Waroquier and V. Van Speybroeck, *ACS Catal.*, 2013, **3**, 2556.
7 M. Ghoussoub, S. Yadav, K. K. Ghurman, G. A. Ozin and C. V. Singh, *ACS Catal.*, 2016, **6**, 7109.
8 M. A. Christiansen, G. Mpourmpakis and D. G. Vlachos, *ACS Catal.* 2013, **3**, 1965.
9 M. A. Christiansen, G. Mpourmpakis and D. G. Vlachos, *J. Catal.*, 2015, **323**, 121.
10 J. F. Lopes, J. C. M. Silva, M. T. M. Cruz, J. W. de M. Carneiro and W. B. De Almeida, *RSC Adv.*, 2016, **6**, 40408.
11 S. Kim, D. J. Robichaud, G. T. Beckham, R. S. Paton and M. R. Nimlos*, J. Phys. Chem. A*, 2015, **119**, 3604.
12 M. Nijemeisland and A. G. Dixon, *AIChE J.*, 2004, **50**, 906.
13 H. A. Jakobsen, H. Lindborg and V. Handeland*, Comput. Chem. Eng.*, 2002, **26**, 333.
14 M. Maestri and A. Cuoci, *Chem. Eng. Sci.*, 2013, **96**, 106.
15 A. Dixon, *Chem. Eng. Sci.*, 2017, **168**, 156.
16 T. Maffei, G. Gentile, S. Rebughini, M. Bracconi, F. Manelli, S. Lipp, A. Cuoci and M. Maestri, *Chem. Eng. J.*, 2016, **238**, 1392.
17 I. Uriz, G. Arzamendi, E. Lopez, J. Llorca and L. M. Gandia, *Chem. Eng. J.*, 2011, **167**, 603.
18 G. Arzamendi, I. Uriz, A. Navajas, P. M. Diéguez, L. M. Gandía, M. Montes, M. A. Centeno and J. A. Odriozola, *AIChE J.*, 2012, **58**, 2785.
19 J. H. Ghouse and T. A. Adams, *Int. J. Hydrogen Energy*, 2013, **38**, 9984**.**
20 J. Petera, L. Nowicki and S. Ledakowicz, *Chem. Eng. J.*, 2013, **214**, 237.
21 J. M. Vanden Bussche and G. F. Froment, *J. Catal.*, 1996, **161**, 1.
22 M. E. Potter, M. E. Cholerton, J. Kezina, R. Bounds, M. Carravetta, M. Manzoli, E. Gianotti, M. Lefenfeld and R. Raja, *ACS Catal.*, 2014, **4**, 4161.
23 M. E. Potter, S. V. Aswegen, E. K. Gibson, I. P. Silverwood and R. Raja, *Phys. Chem. Chem. Phys.*, 2016, **18**, 17303.

View Article Online
DOI: 10.1039/C8CY01564C

24 M. Zhang and Y. Yu, *Ind. Eng. Chem. Res.*, 2013, **52**, 9505.
25 T. K. Phung and G. Busca, *Chem. Eng. J.*, 2015, **272**, 92.
26 H. Knozinger, *Angew. Chem. Int. Ed.*, 1968, **7**, 791.
27 H. Chaing and A. Bhan, *J. Catal.*, 2010, **271**, 251.
28 K. Alexopoulous, M. John, K. Van der Borght, V. Galvita, M. F. Reyniers and G. B. Marin, *J. Catal.*, 2016, **339**, 173.
29 X. Gao, Y. P. Zhu and Z. H. Luo, *Chem. Eng. Sci.*, 2011, **66**, 6028.
30 X. Chen, J. Dai and Z. Luo, *Particuology*, 2013, **11**, 703.
31 X. Chen, A. Vicente, Z. Qin, V. Ruaux, J. P. Gilson and V. Valtchev, *Chem. Commun.*, 2016, **52**, 3512.
32 Q. Sun, N. Wang, R. Bai, X. Chen and J. Yu, *J. Mater. Chem. A*, 2016, **4**, 14978.
33 A. M. Prakash and S. Unnikrishnan, *J. Chem. Soc., Faraday Trans.*, 1994, **90**, 2291.
34 Z. Li, J. Martinez-Triguero, J. Yu and A. Corma, *J. Catal.*, 2015, **329**, 379.
35 G. A. V. Martins, G. Berlier, S. Coluccia, H. O. Pastore, G. B. Superti, G. Gatti and L. Marchese, *J. Phys. Chem. C*, 2007, **111**, 330.
36 L. Smith, A. K. Cheetham, L. Marchese, J. M. Thomas, P. A. Wright, J. Chen and E. Gianotti, *Catal. Lett.*, 1996, **41**, 13.
37 S. Bordiga, L. Regli, C. Lamberti, A. Zecchina, M. Jorgen and K. P. Lillerud, *J. Phys. Chem.* B, 2005, **109**, 7724.
38 C. B. Phillips and R. Datta, *Ind. Eng. Chem. Res.*, 1997, **36**, 4466.
39 J. N. Kondo, D. Nishioka, H. Yamazaki, J. Kubota, K. Domen and T. Tatsumi, *J. Phys. Chem. C*, 2010, **114**, 20107.
40 T. K. Phung, A. Lagazzo, M. A. R. Crespo, V. S. Escribano and G. Busca, *J. Catal.*, 2014, **311**, 102.
41 V. V. Bokade and G. D. Yadav, *Applied Clay Sci.*, 2011, **53**, 263.
42 S. Hopps, S. Sahle, R. Gauges, C. Lee, J. Pahle, N. Simus, M. Singhal, L. Xu, P. Mendes and U. Kummer, *Bioinformatics*, 2006, **22**, 3067-3074.
43 Z. Michalewicz, Genetic algorithms + data analysis = evolution programs, Springer, 2013
44 K. Levenberg, *Quart. Appl. Math.*, 1944, **2**, 164-168.
45 D. Marquardt, *SIAM J. Appl. Math.*, 1963, **11**, 431-441.
46 ANSYS Fluent 17.1, http://www.ansys.com/, December 2017
47 Y. Kawagoe, T. Oshima, K. Tomarikawa, T. Tokusamu, T. Koido and S. Yonemura, *Microfluid. Nanofluid.*, 2016, 20:162.
48 S. Ergun, *Chem. Eng. Prog.*, 1952, **48**, 89.
49 S. V. Patankar and D. B. Spalding, *Int. J. Heat Mass Trans.*, 1972, **15,** 1787.

View Article Online
DOI: 10.1039/C8CY01564C

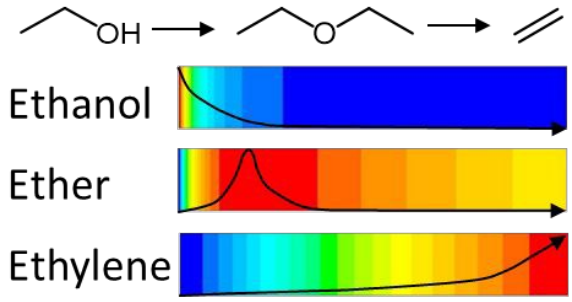

Combining computational fluid dynamics with catalysis gives significant insights into reactor design for sustainable solid acid catalysed processes.